

Supplementary Materials for

Resolving and Weighing the Quantum Orbits in Strong-Field Tunneling Ionization

Here, we provide supplementary materials which include two sections. In the first section, the details of our experiment are shown. In the second section, we show the effect of the Coulomb interaction on the two-color scheme by comparing the results from the strong-field approximation and Coulomb-corrected strong-field approximation.

I. EXPERIMENTAL METHOD

More details of phase-locked Mach-Zehnder interferometer scheme are given in this part. In FIG. S1, the fundamental light is split into two arms of a Mach-Zehnder interferometer. In one arm the fundamental light is frequency doubled in a 300 μm -thick β -barium-borate crystal. The intensity is controlled with a $\lambda/2$ -wave-plate–thin-film-polarizer pair in each arm. The pulse durations (FWHM) of the 800 nm and 400 nm pulses are 40 fs and 110 fs, respectively. To accurately control the relative phase between the fundamental frequency light and the frequency doubled light, we introduce a single longitudinal mode continuous light of 532 nm as the reference light as shown in FIG. S1. The interference fringes, formed after the combined reference lights, are collected by CCD camera in real time. From the offset of the interference fringes, the optical path difference between the fundamental frequency light and the frequency doubled light can be calculated, and then the piezoelectric ceramics of the fundamental frequency light are used for compensation and controlling the relative phase. The phase-locked Mach-Zehnder interferometer scheme can eliminate the influence of airflow disturbance and mechanical vibration on the relative phase. We precisely scan the relative phase of the two-color laser pulse with a step of 0.1π . In each phase measurement result, the phase fluctuation range is $\pm 0.02\pi$.

In the experiment, we calibrate the intensities of the 800-nm and 400-nm pulses separately. For the 800-nm pulse, a coarse estimation of the intensity of the 800-nm field is obtained by the $2U_p$ energy cutoff. Then, the more accurate intensity is calibrated by the positions of the ATI peaks [31]. Due to the ponderomotive shift, the ATI peaks locate at $E_n = n\omega - I_p - U_p$, where n

denotes the number of absorbed photons, ω is the frequency of the 800-nm pulse and I_p is the ionization potential. Using the coarse U_p estimated from the energy cutoff, the absorbed photon number n can be determined and then the accurate value of U_p can be obtained from the shift of the ATI peaks. With this method, the intensity of the 800-nm field is determined to be $\sim 1.2 \times 10^{14}$ W/cm². For the perturbative 400-nm field, the intensity is estimated by comparing the relative-phase-dependent asymmetry of the photoelectron yield in some regions of the PEMDs with the theoretical results from the time-dependent Schrödinger equation (TDSE). The asymmetry is defined as $(Y_L - Y_R)/(Y_L + Y_R)$, where Y_R indicates the normalized photoelectron total yield in the region $p_x \in [p_{x1}, p_{x2}], p_y \in [p_{y1}, p_{y2}]$, and Y_L represents the yield in the corresponding region $p_x \in [-p_{x2}, -p_{x1}], p_y \in [p_{y1}, p_{y2}]$. In FIG. S2, we present an example of the experimental asymmetry $(Y_L - Y_R)/(Y_L + Y_R)$ of the photoelectron with respect to relative phase in the region $|p_x| \in [0.3, 0.8]$ a.u., $p_y \in [-0.2, 0.2]$ a.u.. The data from the TDSE are also shown there. By comparing the amplitude of the relative phase modulation with the TDSE results, the laser intensity of the 400-nm field is estimated to be $\sim 0.3 \times 10^{11}$ W/cm². We note that the intensity of the 400-nm field does not affect our results as long as it is weak enough.

The relative phase in the experiment is also calibrated by comparing the experimental data with the TDSE results, as shown in FIG. S2.

II. THE COULOMB-CORRECTED STRONG-FIELD APPROXIMATION FOR THE PHOTOELECTRON YIELD IN PARALLEL TWO-COLOR FIELD

In our work, the parallel two-color field is given by

$$\mathbf{F}(t; \varphi) = f(t)[-F_1 \cos(\omega_1 t)\vec{x} - F_2 \cos(\omega_2 t + \varphi)\vec{x}], \quad (1)$$

where F_1 and F_2 indicate the electric field amplitudes of the fundamental (FM) driving field and the second harmonic (SH) field, respectively. ω_1 and ω_2 denote their frequencies, respectively. φ represents the relative phase of the two fields and \vec{x} denotes the polarization direction. $f(t)$ is the envelope function of the laser pulse. In our calculations, the laser intensity of the FM field is 1.2×10^{14} W/cm² and that of the SH field is 1.2×10^{11} W/cm². The envelope of the laser pulse is trapezoidal shape envelope with one cycle raise/fall and eight cycles plateau.

For the measured PEMDs, both the long and short orbits contribute. The ionization amplitude

of photoelectron yield is expressed as the coherent superposition of long and short orbits, i.e.,

$$\begin{aligned} |\Gamma(\mathbf{p}; \varphi)|^2 &= |\sqrt{\alpha}\Gamma^L(\mathbf{p}; \varphi) + \sqrt{\beta}\Gamma^S(\mathbf{p}; \varphi)|^2 \\ &= \alpha|\Gamma^L(\mathbf{p}; \varphi)|^2 + \beta|\Gamma^S(\mathbf{p}; \varphi)|^2 + 2\sqrt{\alpha}\sqrt{\beta}|\Gamma^L(\mathbf{p}; \varphi)||\Gamma^S(\mathbf{p}; \varphi)| \cos(\delta\theta). \end{aligned} \quad (2)$$

Here, $|\Gamma^L(\mathbf{p}; \varphi)|^2$ and $|\Gamma^S(\mathbf{p}; \varphi)|^2$ indicate the ionization amplitudes of the long and short orbits, respectively. α and β characterize their contributions. $\delta\theta$ is the phase difference between the long and short orbits.

To identify the contributions of the long and short orbits in the PEMDs, we separately calculate the ionization amplitudes of the long and short orbits based on the strong-field approximation (SFA). Within SFA, the transition amplitude of photoelectron, from the initial ground state to a final state with final momentum \mathbf{p} , is expressed as.

$$|\Gamma(\mathbf{p}; \varphi)|^2 \propto \rho(\mathbf{p}, t_j) e^{-2\text{Im}[\Phi(\mathbf{p}, t_j; \varphi)]}. \quad (3)$$

Here, $\rho(\mathbf{p}, t_j)$ is the pre-exponential factor. It is insensitive to the weak SH field and thus is irrelevant for our present study. So in the following analysis, we drop this factor. In Γ , the classical action is accumulated by

$$\Phi(\mathbf{p}, t_j; \varphi) = - \int_{t_j}^{t_f} \frac{1}{2} \mathbf{v}(t; \varphi)^2 + I_p dt, \quad (4)$$

where $\mathbf{v}(t; \varphi) = \mathbf{p} + \mathbf{A}(t; \varphi)$ represents the kinetic momentum of electron at time t , $\mathbf{A}(t; \varphi) = - \int_{-\infty}^t \mathbf{F}(t; \varphi) dt$ denotes the vector potential of two-color laser field in dipole approximation, and I_p expresses the ionization potential.

In our two-color field, the SH field is much weaker than the FM field, and thus the ionization time t_j of the electron trajectory j of Eq. 4 can be approximately obtained by the saddle-point equation in the FM field, i.e.,

$$[\mathbf{p} + \mathbf{A}_1(t_j)]^2/2 + I_p = 0, \quad (5)$$

where \mathbf{A}_1 represents the vector potential of the FM field.

It should be noted that in SFA, the Coulomb interaction of the electron and parent ion has not been taken into account, thus the correspondence between the final momentum and ionization time from Eq. 5 is inaccurate. In our study, the ionization time is the decisive factor for the relative phase dependence of the photoelectron yield. So, we have to correct the ionization time by including the effect of the Coulomb interaction. In previous studies, it has been demonstrated that the

Coulomb-corrected SFA can depict the photoelectron momentum map precisely. So, we employ the Coulomb-corrected SFA to include the influences of Coulomb interaction in the followings.

In the FM field, the Coulomb force is taken into account by the electronic motion equation,

$$\ddot{\mathbf{r}} = d\mathbf{v}/dt = -\mathbf{F}_1 - \mathbf{r}/|\mathbf{r}|^3. \quad (6)$$

Now, the canonical momentum \mathbf{p} does not conserve, $\dot{\mathbf{p}} = d[\mathbf{v} + \mathbf{A}_1(t)]/dt = -\mathbf{r}/|\mathbf{r}|^3$. Equation 5 determines the relationship of the ionization time and “initial” momentum. With Eq. 6, we could establish the relation of the “initial” momentum and the final momentum (the measured momentum). Then, the relationship between the measured momentum and the ionization time is established. Figure S3 shows the ionization times of the long and short orbits with and without the Coulomb correction. The Coulomb interaction induces notable differences in the ionization times.

Accordingly, the ionization amplitude of Eq. 3 in the Coulomb-corrected SFA is rewritten as

$$|\Gamma(\mathbf{p}; \varphi)|^2 \propto e^{-2\text{Im}[\Phi(\mathbf{p}, t'_j; \varphi)]}, \quad (7)$$

where t'_j is the Coulomb-corrected ionization time. With this equation, we separately calculate the relative phase dependences of the photoelectron yield from the long and short orbits, as indicated in FIG. S4. It is shown that the photoelectron yield oscillates with the relative phase of the two-color field. Here, the results from the SFA are also shown for comparison. It is clearly seen that there is a remarkable shift between the optimal phases (where the photoelectron yield maximizes) from SFA and Coulomb-corrected SFA for both of the long and short orbits. We note that the relation of the optimal phase and ionization time obtained in our numerical calculations is in consistent with the results given by Eq. 6 of [30].

We should mention that for the long orbit the electron wave packet is split into two pathways, when it is driven back to the parent ion after tunneling ionization. One suffers a near-forward rescattering and one without rescattering. For the momentum region we consider in our study, this re-collision is soft re-collision, and the ionization times for the electron with the same final momentum for these two pathway are nearly the same. Thus the relative phase dependences of the photoelectron yield from these two pathways of the long orbit are the same. These results are shown in FIG. S5. The optimal phases for the two pathways of the long orbit are the same, and thus we don't need to consider the near-forward rescattering process when we retrieve the relative contributions of the long and short orbits.

For the experimentally measured PEMDs, both of the long and the short orbits contribute, and the relative phase dependence of the photoelectron yield can be described by Eq. 2. Due to the

laser focal volume effect, the interference pattern is smeared out. Therefore, the interference term is not visible, and we ignore the interference term in Eq. 2.

To check the validity of this point, we compare the results with and without the interference term using the data from SFA. The results are shown in FIG. S6. We extract the phases φ_m from the SFA data where the interference term is kept and the result is shown in FIG. S6(d). We then exclude the interference term in PEMD and extract the phase φ_m , the result is shown in FIG. S6(c). The agreement of the obtained phases φ_m between these two treatments is remarkable. It means that the responses of the photoelectron yields with and without interference term to the SH field are the same. Thus, The interference term does not affect the obtained relative contribution of long and short orbits, and thus the interference term can be canceled out safely in our scheme. As shown above, the first two terms in Eq. 2 exhibit the cosine-like dependence on the relative phase of the two-color field, and so, the experimental data can be approximately described by

$$\cos(\varphi - \varphi_m) = \alpha \cos(\varphi - \varphi_m^L) + \beta \cos(\varphi - \varphi_m^S), \quad (8)$$

where φ_m^L and φ_m^S are the optimal phases of the long and short orbits, obtained with the Coulomb-corrected SFA.

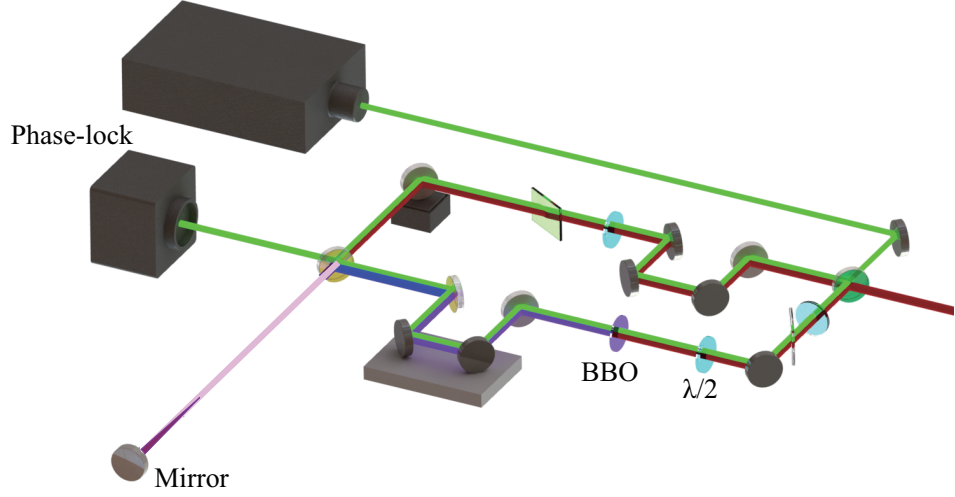


FIG. S1: Schematic view of phase-locked Mach-Zehnder interferometer scheme.

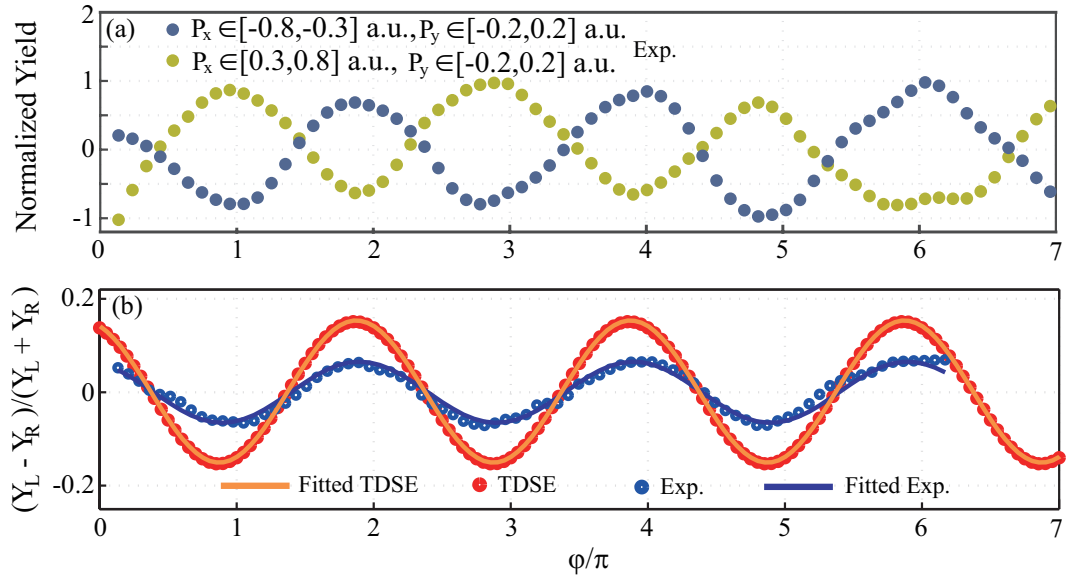


FIG. S2: (a) The normalized photoelectron total yield Y_R (green curve) and Y_L (blue curve) for $p_x \in [0.3, 0.8]$ a.u., $p_y \in [-0.2, 0.2]$ a.u. and $p_x \in [-0.8, 0.3]$ a.u., $p_y \in [-0.2, 0.2]$ a.u. as functions of φ , respectively. (b) $(Y_L - Y_R)/(Y_L + Y_R)$ obtained from experiment (blue curve) and TDSE results (red curve).

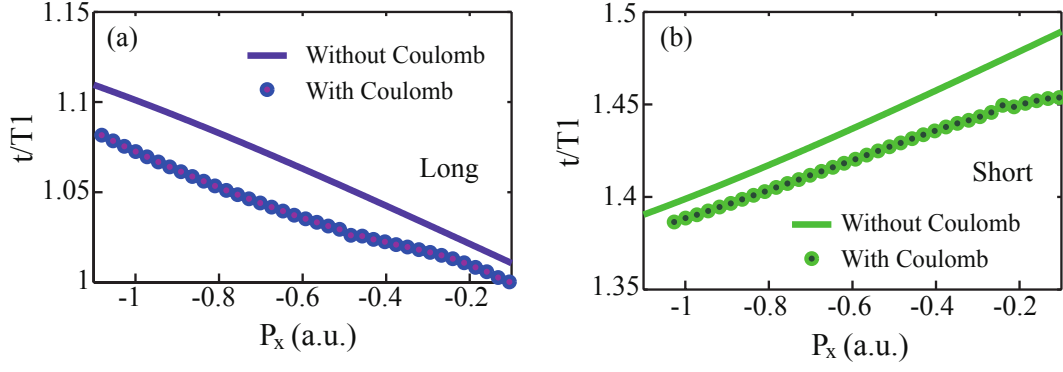


FIG. S3: (a)-(b) The ionization times of the long and short orbits as function of p_x . The solid curves and the circles indicate the results without and with the Coulomb correction, respectively.

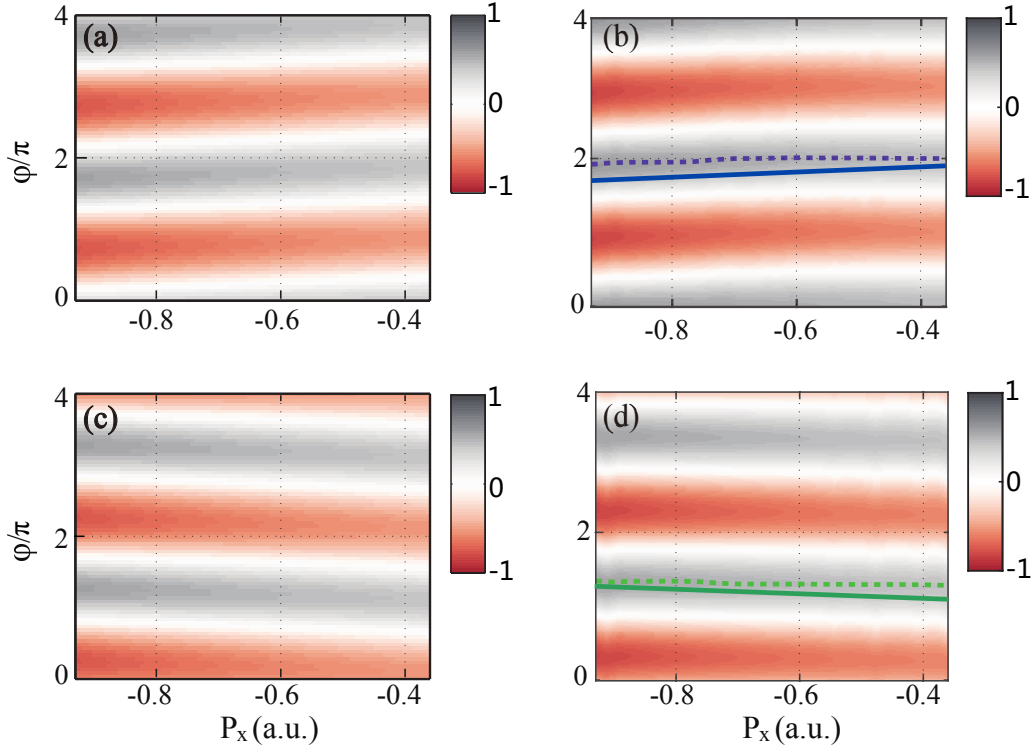


FIG. S4: The NDs at $p_y = 0$ as functions of relative phase. The upper and the lower rows correspond to the results for the long and the short orbits, respectively. In the left column, the effect of the Coulomb correction is not taken into account, and in the right column, the Coulomb correction has been included. The dashed curves in (b) and (d) show the optimal phases of the NDs, and the solid curves indicate the optimal phases of the NDs in (a) and (c).

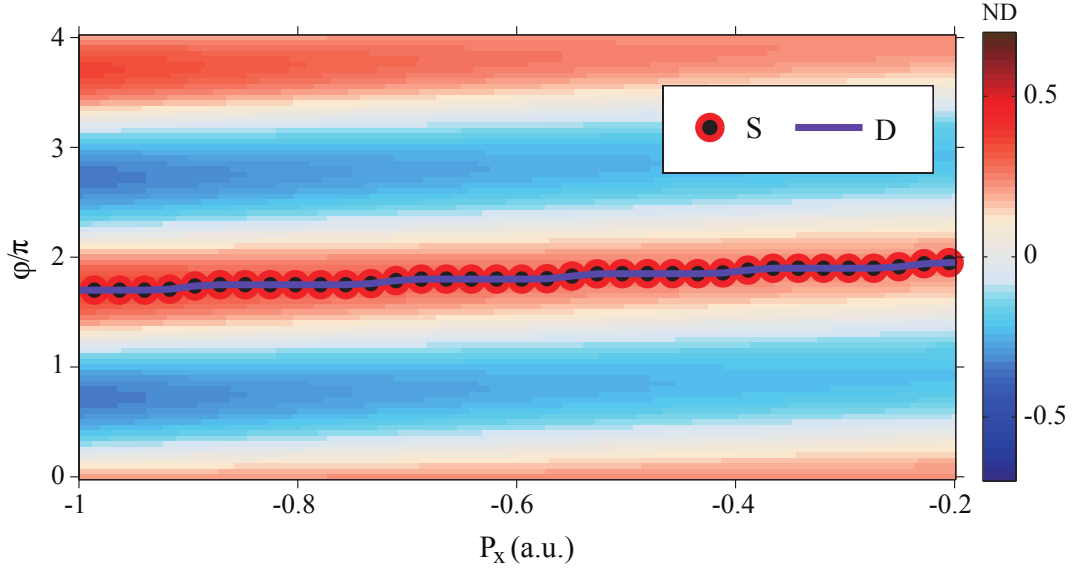


FIG. S5: The NDs at the cut of $p_y = 0$ as functions of φ for the long orbit. The solid purple curve indicates the optimal phase of the direct electrons and the red circles show that of the rescattering electrons.

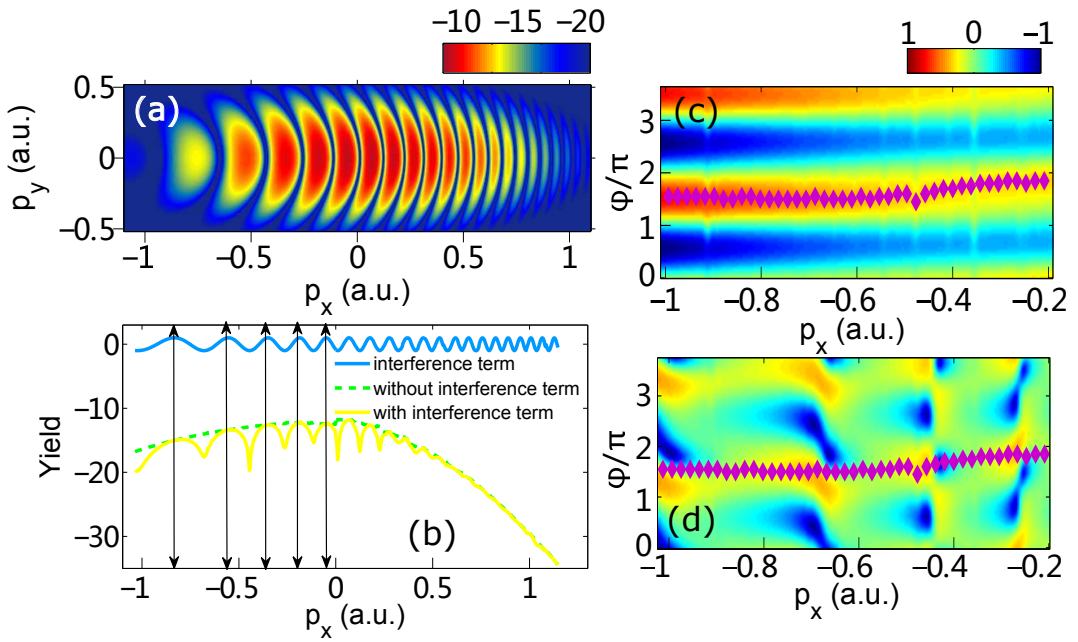


FIG. S6: (a) The ionization amplitude $|\Gamma(\mathbf{p}; \varphi)|^2$ obtained by the coherent superposition of the long and short orbits. (b) the cut of $|\Gamma(\mathbf{p}; \varphi)|^2$ at $p_y = 0$ with (solid yellow curve) and without (dashed green curve) interference term. The solid blue curve shows the interference term $\cos(\delta\theta)$ at $p_y = 0$. (c) and (d) NDs for $p_y = 0$ at different relative phase. In (c) the interference term is not included, while in (d) it is contained.